

# 1

## Waveguides for Micro-Magnetic Resonance

*Ali Yilmaz and Marcel Utz*

### 1.1

#### Introduction

In nuclear magnetic resonance, a system of nuclear spins exposed to a static magnetic interacts with an oscillatory field, usually in the radio frequency range [1]. In most NMR setups, including all in all commercially available NMR spectrometers, coherent transitions between spin states are detected by a voltage induced into a conductor surrounding the sample. While other have their advantages in certain cases, inductive detection has proven to be both robust and easy to implement.

The earliest demonstrations of nuclear magnetic resonance, pioneered by Rabi [2], have relied on the deflection atomic beams in inhomogeneous fields according to the spin state, rather than on inductive detection. However, NMR only became a widely used tool for chemistry after the invention of the direct induction method, independently discovered by Bloch [3] and by Purcell, Torrey, and Pound [4] in 1946.

The same conductor that detects the nuclear spin precession can also be used for its excitation. Particularly in the context of the Fourier spectroscopy method [5], this has become very useful. It is relatively easy to expose a sample to an oscillatory magnetic field by surrounding it with a suitable conductor, through which an alternating current is sent at the appropriate frequency. The precessing spins induce a measurable voltage in the same conductor. There are technical problems to be solved that arise due to the high power that is needed in some cases for excitation, while the induced voltages are very small and require exquisitely sensitive receivers. It is not uncommon for excitation RF power to approach several kW, whereas the power available for spin detection is many orders of magnitude lower.

The earliest inductive NMR systems have almost exclusively relied on solenoid coils as excitation/ detection systems. As the applications of NMR have diversified, and new technologies have become available, other geometries have been explored. In the 1970s, electromagnets with planar gaps were replaced by superconducting solenoids, which offered higher fields and better stability. To facilitate loading samples axially through the magnet bore, saddle coils and related resonator geometries have been developed. At the same time, magnetic resonance imaging, in particular

for medical applications, brought the need to accommodate much larger samples.

Today, most detectors used in NMR spectroscopy follow a cylindrical form factor, optimised for standard NMR sample tubes of 5 mm or 10 mm diameter. Some special applications, though, require a different geometry, and in particular, the study of thin films, membranes, and interfaces is inefficient in cylindrical detectors, and various alternative detector geometries have been explored. For example, flattened solenoid probes have been developed for the study of membrane proteins under solid-state NMR conditions [6].

The present chapter is concerned with the use of planar waveguides, such as striplines and microstrips, as inductive detectors for NMR spectroscopy and imaging. As will become clear in the following, such structures readily lend themselves to miniaturisation, since they can be fabricated using efficient lithographic techniques. However, they were introduced as detectors in magnetic resonance imaging long before their potential for micro-NMR was discovered.

As the magnetic fields, and, correspondingly, the Larmor frequencies used in MRI scanners have increased, uniform penetration of the radio frequency magnetic fields into the tissue has become more and more difficult. Since biological systems contain ionic solutions, non-conservative electric fields arising in the detector system need to be shielded from getting in contact with the tissue. The dielectric losses incurred from interaction between these electric fields and the tissue degrade the sensitivity of the detection, but they also lead to excessive power deposition in the tissue during excitation. As a solution, surface coils for localised MR imaging of human subjects based on circular or quadratically laid out strip lines have been proposed [7].

Compared to many other spectroscopic techniques, NMR suffers from a major drawback: its relative insensitivity. While UV/VIS techniques, in particular fluorescence, can detect signals from single molecules with relative ease, NMR typically requires of the order of  $10^{15}$  spins to resonate within a narrow bandwidth (1 Hz or so) in order for the signal to be measurable. The design of NMR detectors that offer optimal sensitivity has therefore been a long-standing research topic. Sensitivity is determined by the signal/noise ratio that can be obtained within a specified amount of time from a defined number of spins. Inductive detectors based on resistive metals invariably produce thermal noise. Under optimal conditions, where all non-intrinsic sources of noise have been eliminated by shielding, the blackbody radiation of the resonator structure itself leads to a noise voltage spectral density which is essentially independent of frequency, and scales proportionally to the square root of the ohmic resistance of the detector.

The relationship between the NMR spin precession and the induced voltage signal has been discussed by Hoult and Richards in terms of the correspondence principle [8]. The induced signal strength from a single spin depends on the normalised magnetic field at the location of the spin that the detector circuit produces per unit current flowing in it. Hence, efficient detectors need to be designed such that the magnetic field they generate is maximal. This conflicts with the requirement of low ohmic resistance, which is important to keep the noise voltage small, and a compromise between the two must be found in practice.

It has been well known for about two decades that the mass sensitivity (i.e., the

signal/noise ratio per spin and per bandwidth) of inductive detectors is roughly inversely proportional to the detector size. This can be rationalised by examining the normalised magnetic field and the radio frequency resistance of a particular detector geometry as a function of its overall dimensions. For example, the magnetic field generated at the centre of a circular loop of diameter  $d$  made of a wire of thickness  $h$  is given approximately by  $H/I = 1/(\pi d)$ . If the geometry is scaled by a factor  $\alpha$ ,  $H/I$  therefore scales as  $\alpha^{-1}$ . At typical NMR frequencies, the skin depth in Cu amounts only to a few  $\mu\text{m}$ . Therefore, as both the wire diameter and the loop diameter are scaled by the same factor  $\alpha$ , the resistance of the structure remains roughly constant, as long as the wire diameter remains larger than the skin depth. As a result the signal to noise ratio for a given number of spins is expected to scale roughly as  $1/\alpha$ . A similar argument can be made for solenoid coils and other detector geometries.

Microfluidics represents a rapidly expanding field of science and technology. The underlying idea is borrowed from micro-electronics: to integrate complex functionality in a mostly two-dimensional layout, making use of efficient lithographic fabrication technologies. This lab-on-a-chip (LoC) approach has proven especially fruitful in enabling total analysis systems, which integrate sample preparation, chromatographic separation, and detection on single chip platform [10].

Since lithographic techniques allow the accurate reproduction of complex and very highly resolved features, microfluidic systems can be designed to mimic highly complex environments with great control and accuracy. This enables the culture of biological systems under artificial and highly controlled conditions, while closely mimicking the natural environment. This has become an invaluable tool for the study of differentiated cells, their development, and the interplay between different cell types.

NMR spectroscopy is uniquely suited to observe metabolic processes in live systems. It therefore has great potential as an observation tool in microfluidic culture assays. However, in spite of significant efforts, its use in the context of microfluidic devices is not yet widespread. There are a number of reasons for this. On the one hand, the planar geometry of microfluidic devices is not easily combined with common NMR detectors, which are typically designed for a cylindrical sample. Another limitation is the poor sensitivity of NMR, which is exacerbated by the small sample amounts typically available in microfluidic systems. Stripline and microstrip detectors are of particular interest in this context, since they inherently follow a planar geometry, and they can offer extremely high mass sensitivity, as will be discussed in detail in the following.

Looking into the future, transmission-line based detector geometries offer significant potential for further advances in miniaturisation. Their fabrication using lithographic techniques is straightforward, in contrast to intrinsically three-dimensional geometries such as solenoids, and there is no reason why they could not be successfully applied to detectors an order of magnitude or more smaller than the ones that have been demonstrated so far. Another exciting possibility is the use of transmission line detectors in travelling wave mode, rather than as resonators carrying standing waves. Travelling wave NMR, which has been demonstrated in the context of magnetic resonance imaging and (macroscopic) NMR spectroscopy, could have significant advantages at the micro scale, since it allows the spatial separation of the

sample and the detection circuitry.

## 1.2

### Waveguides: Theoretical Basics

#### 1.2.1

#### Propagating Electromagnetic Modes

The presence of conducting surfaces imposes boundary conditions on the free propagation of electromagnetic waves. The electric field vector must stay perpendicular to the surface of an ideal conductor, while the magnetic field vector is required to stay parallel. Wave guides are long structures of an insulator (called the dielectric) surrounded by conducting surfaces, usually with a constant cross section. Electromagnetic waves of different types (modes) can propagate in the longitudinal direction in such structures. They are classified as transverse electric (TE) or transverse magnetic (TM) waves [11]. In TE waves, the electric field has no component in the longitudinal direction, while the longitudinal magnetic field vanishes for TM waves.

In waveguides bounded by a single conductor, such as a rectangular or a cylindrical tube, wave modes only propagate if the wave length is not significantly larger than the lateral dimensions of the conductor. This leads to a minimum frequency for each propagating mode, which is often referred to as the cutoff frequency. Also, the relationship between the wavelength and the frequency for TE and TM modes is non-linear, leading to dispersion.

In addition to TE and TM waves, another type of propagating mode becomes available if the walls of the waveguide are divided into several (at least 2) mutually insulated sections. In this case, an oscillatory voltage can be sustained within the cross section between the separate conductors. Under these conditions, propagating modes exist with *both* the electric and magnetic fields transverse. Such TEM modes do not have a cutoff frequency, and in general exhibit a linear relationship between wavelength and frequency.

The frequencies of interest in magnetic resonance lie below 1.5 GHz. With usual dielectrics, this yields wave lengths of 20 cm or more, and hollow waveguides supporting TE or TM modes for these frequencies would be very unwieldy. Therefore, TEM modes are commonly used in order to transport NMR signals, mostly in coaxial cables. By contrast, electron paramagnetic resonance (EPR), with frequencies up to several hundred GHz, often relies on rectangular waveguides.

In the present context, we are interested in the use of waveguides not only for carrying RF signals between different components of the experimental setup, but also for inductive detection of the nuclear spin precession. Fig. 1.1 shows some examples of wave guide cross sections capable of supporting TEM modes which have been used successfully as NMR detectors. Planar wave guide structures such as the microstrip (Fig. 1.1b) and the stripline (Fig. 1.1c) are conveniently implemented on printed circuit boards, [12] and are very commonly used in the design of radio frequency and microwave circuits.

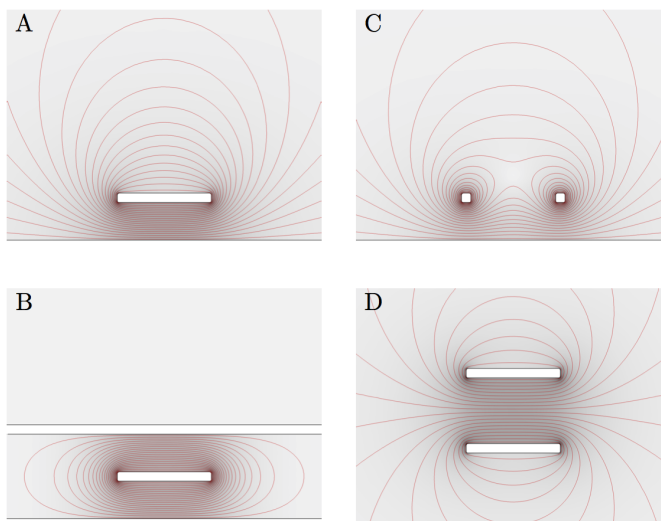


**Figure 1.1** Cross section of some typical planar transmission line geometries, including magnetic field lines of the TEM mode. A: microstrip, B: stripline, C: microslot, D: parallel plate transmission line

### 1.2.2

#### Characteristic Impedance and Transport Characteristics

For TEM modes, it is possible to attribute a current and a voltage amplitude to the travelling wave by integrating along the electric and magnetic field lines in the cross section, respectively. While the absolute voltage and current amplitudes depend on the power transported by the wave, their ratio (measured in  $\Omega$ ) is a constant defined purely by the cross section geometry and the dielectric and magnetic properties of the insulating medium. This ratio is known as the characteristic impedance  $Z_0$  of the wave guide. Coaxial cables are commonly designed for a characteristic impedance of  $50\Omega$ .

### 1.2.3

#### Theory of TEM Wave Modes

Maxwell's curl equations couple the magnetic field  $\mathbf{H}$  and the electric field  $\mathbf{E}$ . If we assume a harmonic time evolution of the fields with angular frequency  $\omega$ , they become

$$\nabla \times \mathbf{H} = j\omega\epsilon\mathbf{E} \quad (1.1)$$

$$\nabla \times \mathbf{E} = -j\omega\mu\mathbf{H} \quad (1.2)$$

where  $j = \sqrt{-1}$  is the imaginary unit, and  $\epsilon$  and  $\mu$  represent the electric permittivity and magnetic permeability of the insulating medium, respectively. In order to analyse a TEM mode, we assume the axis of the transmission line to be aligned with the  $z$  direction. The two curl equations can be combined to the Helmholtz equation

$$(\nabla^2 + k^2)\mathbf{E} = 0, \quad (1.3)$$

where  $k = \omega\sqrt{\mu\epsilon}$  is the wave number. If we assume the transverse components of the electric field to depend harmonically on  $z$ , proportionally  $e^{-jkz}$ , it is easily shown that they satisfy Laplace's equation, i.e.,

$$\left( \frac{\partial^2}{\partial x^2} + \frac{\partial^2}{\partial y^2} \right) E_{x,y} = 0. \quad (1.4)$$

A similar argument leads to the same result for the transverse magnetic field. The electric and magnetic field distribution in the cross section of a transmission line are therefore both solutions to Laplace's equation, but they obey different boundary conditions. For the electric field, we have  $\mathbf{E} \cdot \mathbf{n} = 0$  at the conductor surface, and the magnetic field satisfies  $\mathbf{H} \times \mathbf{n} = 0$ , where  $\mathbf{n}$  is the surface normal. It is useful to note that the field distributions follow the same laws as static fields. In particular, this means that the field distribution for a TEM mode is *independent of the frequency*. TEM transmission lines are therefore inherently broad-band devices, with no lower limit to the frequencies they can carry. In theory, there is no upper limit for the propagation of the TEM mode either; however, the excitation of TE and TM modes complicates the situation at very high frequencies. For this reason, coaxial transmission lines are only used up to frequencies of several GHz.

#### 1.2.4

#### Modelling of TEM modes

Since the transverse electric and magnetic field distributions for TEM modes are solutions of the two-dimensional Laplace equation, they are easily computed for any geometry using a finite element or finite difference approach. Since the electric field is curl-free, it can be represented as the gradient of an electrostatic potential  $\phi(x, y)$ , which satisfies the (scalar) Laplace equation. Computing the transverse field distribution therefore reduces to a simple Dirichlet problem, where fixed potential values must be attributed to the conductor surfaces:

$$\nabla^2 \phi(x, y) = 0 \quad \text{on } B, \quad \phi = V_{1,2,\dots} \quad \text{on } \partial B_{1,2,\dots}, \quad (1.5)$$

where  $B$  denotes the dielectric cross section, and  $\partial B_{1,2,\dots}$  represent the conductor surfaces, and  $V_{1,2,\dots}$  are the electrical surface potentials. The electric field of a propagating TEM mode is then given by

$$\mathbf{E} = e^{-jkz} \left( -\frac{\partial \phi}{\partial x}, -\frac{\partial \phi}{\partial y}, 0 \right), \quad (1.6)$$

where  $\gamma = \alpha + jk$  is the propagation constant, which describes both the oscillatory propagation of the wave in the  $z$  direction with wave number  $k$  and its gradual attenuation with decay constant  $\alpha$ .<sup>1)</sup>

The magnetic field distribution is easily found using the the curl equations:

$$\mathbf{H} = e^{-\gamma z} \left( \frac{1}{\eta} - \frac{j\alpha}{\omega\mu} \right) \left( \frac{\partial\phi}{\partial x}, -\frac{\partial\phi}{\partial y}, 0 \right), \quad (1.7)$$

where the characteristic impedance of the medium  $\eta$  is given by

$$\eta = \sqrt{\frac{\mu}{\epsilon}}. \quad (1.8)$$

Note that in the case of  $\alpha = 0$ , the magnetic and the electric field are *in phase*, whereas a positive attenuation constant  $\alpha > 0$  leads to the magnetic field phase lagging behind the electric field. The time-averaged power transported by the TEM wave is given by real part the Poynting vector as

$$\Re(\mathbf{S}) = \frac{1}{2} \Re(\mathbf{E} \times \mathbf{H}^*) = p_t \hat{\mathbf{z}}, \quad (1.9)$$

where the cross-sectional density of power  $p_t(x, y)$  is

$$p_t(x, y) = \frac{e^{-2\alpha z}}{2\eta} \left[ \left( \frac{\partial\phi}{\partial x} \right)^2 + \left( \frac{\partial\phi}{\partial y} \right)^2 \right]. \quad (1.10)$$

The relative power loss per unit length is therefore given by

$$\frac{1}{p_t} \frac{\partial p_t}{\partial z} = -2\alpha. \quad (1.11)$$

At every cross section of the transmission line, it is possible to compute the electrical potential difference between the two conductors by a path integral between the conductor surfaces

$$V(z) = \oint_1^2 \mathbf{E}(x, y, z) \cdot d\mathbf{s}, \quad (1.12)$$

Similarly, the current flowing in the conductor can be obtained using Ampere's law

$$I(z) = \oint \mathbf{H}(x, y, z) \cdot d\mathbf{s}, \quad (1.13)$$

where the integration path in this case is a closed loop around the conductor.

It is easily shown that the voltage and current thus obtained satisfy the equations

$$\frac{d^2V}{dz^2} = \gamma^2 V(z) \quad (1.14)$$

$$\frac{d^2I}{dz^2} = \gamma^2 I(z). \quad (1.15)$$

1) It should be noted that the foregoing treatment is only strictly exact in the limit  $\alpha \ll k$ . However, for transmission lines composed of polymer dielectrics and good conductors, this is almost always true to a good approximation.

These equations are useful to describe the behaviour of transmission lines when integrated into electrical circuit networks. In general, they can be solved by a superposition of two waves travelling in opposite directions:

$$V(z) = V_0^+ e^{-\gamma z} + V_0^- e^{\gamma z} \quad (1.16)$$

$$I(z) = I_0^+ e^{-\gamma z} + I_0^- e^{\gamma z}. \quad (1.17)$$

The ratio

$$Z_0 = \frac{V_0^+}{I_0^+} = \frac{V_0^-}{I_0^-} \quad (1.18)$$

is known as the characteristic impedance of the transmission line. Its value depends entirely on the geometry of the transmission line cross section and on the dielectric and magnetic properties of the insulator.

#### 1.2.4.1 Losses in Transmission Lines

There are two main contributions to the power losses in a transmission line. On the one hand, there are dielectric losses due to the repeated polarisation and depolarisation of the insulating medium. These are proportional to the magnitude of the electric fields. The dielectric properties of most insulator materials are only very weakly frequency dependent; the dissipated power therefore tends to be proportional to the frequency. The dielectric dissipation of a material can be expressed by an imaginary component in its dielectric permittivity  $\epsilon = \epsilon' - i\epsilon''$ . Often, the loss tangent, defined as  $\tan \delta = \epsilon''/\epsilon'$  is used in order to characterise the material. A second (and, in the present context, often dominant) source of losses is the finite conductivity of the metallic surfaces. A plane electromagnetic wave impinging on an imperfect conductor penetrates into it only to a finite depth  $\delta_s$ , known as the skin depth. This is because the tangential component of the magnetic field at the boundary induces in the surface a current which cancels the magnetic field deeper inside the metal. Since this current is sustained against a finite ohmic resistance, it dissipates power from the electromagnetic wave. If the lateral dimensions of the transmission line are much larger than the skin depth, it is possible to express the average dissipated power per unit surface area as

$$P_\delta = \frac{1}{2} |H_{\parallel}|^2 R_s, \quad (1.19)$$

where  $R_s$  is the surface resistance of the metal. It depends on the conductivity  $\sigma$  and the skin depth  $\delta_s$  as

$$R_s = \frac{1}{\sigma \delta_s} = \sqrt{\frac{\omega \mu}{2\sigma}}. \quad (1.20)$$

For pure Cu,  $\sigma = 5.9 \cdot 10^7 \text{ S/m}$ , which translates into a surface resistance of about 10 mΩ at 100 MHz, and about 35 mΩ at 1 GHz. The losses lead to a gradual attenuation of a travelling TEM mode, as reflected in the real part of the propagation constant  $\gamma$ .

### 1.2.5

#### **Magnetic Fields in Planar TEM Transmission Lines**

The magnetic and electric field distributions of the TEM mode in some planar transmission line geometries are shown in Fig. 1.1. The stripline (Fig. 1.1A) consists of a single conductor symmetrically bounded between two ground planes. The magnetic field lines encircle the central conductor, producing two areas of very high field homogeneity which can be used as sample locations for NMR spectroscopy. The microstrip, shown in Fig. 1.1B, exhibits a similar field geometry. However, since there is only a single ground plane, the magnetic and electric fields penetrate into the free space above. This is less pronounced in practice than in the idealised computation shown here, since the dielectric constant of the insulator means that the electric field remains partially captured inside it. Nonetheless, the open geometry can lead to radiation losses, which must be kept to a minimum by external shielding. The difference in dielectric properties between the insulator and the surrounding air also means that the propagating mode in a microstrip is not strictly a TEM mode, and maintains some TE character. This means that the relationship between the frequency and wavelength is not exactly linear, leading to frequency dispersion.

Fig. 1.1C shows a microslot line. In this case, there are two independent conductors, which can in principle carry different electrical potentials. This geometry is therefore capable of supporting more than one TEM mode. However, in the present context, only the common mode shown in Fig. 1.1C is of interest. Compared to the similar microstrip geometry, the magnetic field is concentrated in the space immediate above the pair of conductors.

Finally, Fig. 1.1D shows a parallel plate transmission line (PTL). In this case, the two conductors are symmetrically placed above and below the centre line. The field lines extend into space on both sides of the structure, and are compressed into a region of high field homogeneity in between the two conductors.

### 1.2.6

#### **Transmission Line Detectors and Resonators**

According to the correspondence principle, the sensitivity of an NMR detector is directly related to the magnetic field it generates at the location of the sample per unit current [13]. In a transmission line detector, sensitivity is therefore maximised if the lateral dimensions are chosen as small as possible, and if the region of the largest magnetic field in the TEM mode is filled with the sample. On the other hand, transmission lines with small cross sections tend to be more lossy. Many detector geometries therefore constrict the width of the transmission line at the site of the sample.

In order to optimise the coupling of the detector to the spectrometer transmitter and receiver circuits, it is necessary to match its impedance to the standard impedance, usually  $50\Omega$ . This is most commonly achieved by tuning the detector to a resonance frequency very slightly above the desired Larmor frequency, and then nulling the resulting positive reactance with a series capacitor.

A transmission line stub of length  $l$  with open ends (infinite termination impedance) will support a manifold of eigenmodes, with frequencies that correspond to standing waves with current nodes at the ends, i.e., an integer number of half waves must fit into  $l$ . The standing waves at these frequencies exhibit voltage nodes at the locations of the current anti-nodes. This is convenient in NMR spectroscopy, because the most sensitive location of the resonator (at the magnetic field maxima) are automatically the ones where the electric field amplitude vanishes. Well-designed resonant transmission line probes therefore exhibit only minimal sample heating, and are largely immune to quality factor degradation through dielectric losses.

Resonators can also be realised with other terminations. Often, one end of the transmission line is short-circuited, rather than left open. This leads to a current anti-node at the shorted end. In some cases, it is desirable to achieve as uniform as possible a current distribution throughout the length of the transmission line detector. This can be achieved by terminating both sides with a capacitor. The desired eigenmode is then characterised by one capacitor being discharged while the other is charged, and vice versa. The current amplitude in the transmission line is then almost constant over its length. Obviously, only frequencies below the fundamental mode of the corresponding open-ended transmission line resonator can be accessed in this manner.

### 1.3

#### Designs and Applications

##### 1.3.1

##### **Microstrip NMR Probes in MRI**

Microstrips were introduced into magnetic resonance imaging long before their benefits for micro-scale NMR spectroscopy were realised. For example, Bridges proposed a resonator based on a cylindrical arrangement of microstrips inside a common ground cylinder [14]. This can be seen as a short piece of multi-conductor transmission line, capable of supporting many different TEM modes. As Bridges showed, one of these is characterised by a highly homogeneous  $B_1$  field on the inside.

A similar design has been described later by Bogdanov and Ludwig [15]. The arrangement and its eigenmode is similar to the birdcage coil [16], which has become the mainstay of volume detectors in MRI. As the magnetic fields available for MRI increased, it became more important to limit the exposure of the human subject to radio frequency electric fields. RF heating of the sample, and, concomitantly induced noise, become more difficult to manage at higher magnetic fields. With the advent of 3.5 T and later 7 T MRI scanners, strategies for limiting the penetration of electric fields into the sample and for reducing radiation losses were needed. Zhang et al [7, 17] demonstrated that single square loop surface coils made from a microstrip provided significant advantages over conventional loop coils of comparable dimensions. These loops consist of a microstrip designed to support a  $\lambda/4$  standing wave, with either an open or a shorted end. At higher fields, the quarter wavelength re-

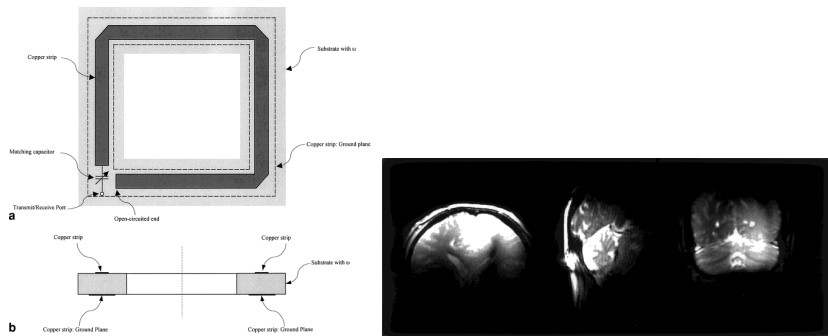


**Figure 1.2** Single-turn microstrip transmission line surface coil for MRI at 7 T (left), and images of the human brain (right). Reprinted with permission from [7].

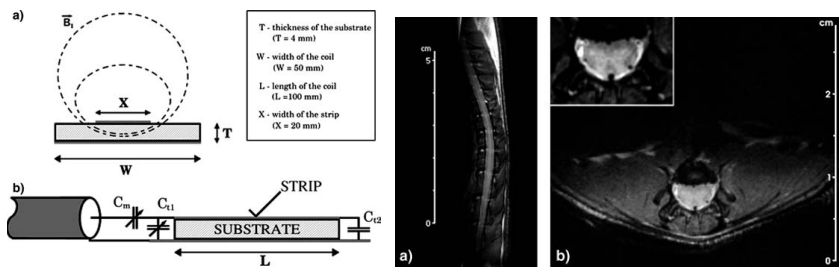


**Figure 1.3** Microstrip transmission line resonator, and images of the rat spine (right). Reprinted with permission from [19].

quirement limits the size of the coils that can be built on this basis. However, planar multi-loop coils supporting higher-order modes ( $3\lambda/4$  and higher) have also been demonstrated [18].

Zhang et al. developed an elegant version of the stripline volume detector, in which the coupling between the lines is accomplished by simply dividing the backplane conductor into two halves in the axial direction of the cylinder. This avoids the need to connect each strip separately through a matching network [20]. Standing wave microstrip resonators have been used for micro-imaging of the rat spinal cord at 4.7 T with a resolution of 0.15mm [19], as shown in Fig. 1.3.

Collections of microstrips can be arranged in a three-dimensional fashion to create volume coils [21]. Actively de-tuneable transmission-line head coils, in which the individual microstrips can be shunted to the ground plane by means of DC-biased PIN diodes [22], allow the simultaneous use of localised receiver coils inside the volume resonator without mutual coupling artefacts. Lee et al. proposed an array of planar microstrips [23, 24] for phased-array detection [25, 26]. Their design exploits an intriguing property of identical parallel and coplanar microstrips: standing wave

modes in adjacent strips are automatically decoupled from each other by symmetry. Phased microstrip array detectors have since been used successfully as external coils for prostate imaging [27], and an array of mutually decoupled microstrip loops has been used by Adriany et al for parallel acquisition and individual control of RF phases and amplitudes in a human head coil at 7 T [28]. It should be noted that in cylindrical and other non-planar arrangements, identical parallel microstrips are no longer automatically decoupled. Decoupling can be achieved either capacitively, or inductively [29]; the latter approach has the advantage that the coupling and decoupling mechanisms follow the same frequency dependence, i.e., the decoupling is broad-band.

The properties of microstrip resonators and other MRI detector geometries have been compared in numerical and in some cases experimental studies by several authors [30–32]. Wang and Shen [30] compared the sensitivity, power deposition, and field distributions for birdcage, microstrip, and TEM coils at 7T by finite element computations. They found microstrip coils to provide superior SNR while depositing less power into the tissue than birdcage or TEM resonators. Ipek et al. [32] experimentally compared a radiative dipole antenna with a microstrip resonator of similar dimensions for prostate imaging at 7T. The radiative antenna design is optimised to produce a Poynting vector perpendicular to the plane of the antenna, in order to radiate into the tissue and reach deeper lying structures. By contrast, the microstrip resonator does not radiate efficiently, the main direction of its Poynting vector is in the axial direction (and its time average vanishes due to the standing wave resonance). Ipek et al. found this to be reflected in deeper reaching B1 fields for the antenna. However, the power deposited in the tissue was lower, and the SNR for areas closer to the receiver was higher for the microstrip resonator.

### 1.3.2

#### **Microfluidic NMR**

Micro-solenoid coils, with diameters more than an order of magnitude smaller than conventional detectors, exhibit very high mass sensitivity [33–35], and thus allow direct combination of NMR detection with chromatographic separation techniques such as capillary electrophoresis [36–38] and high-pressure liquid chromatography [39]. Solenoidal micro coils have also been used successfully for micro-imaging [40, 41], achieving resolutions approaching the single cell length scale.

In solid-state NMR, micro coils have been used for statically, for example for studying spider silk [42], but also under Magic-angle spinning (MAS) NMR has been made possible by attaching the micro-scale sample to a conventional MAS rotor, and surrounding it by a micro-solenoid [43]. Another possibility is to insert a tuned micro coil into the MAS rotor, and spinning it together with the sample. The coil is then inductively coupled to the macroscopic probe coil [44, 45].

In recent years, MAS probes capable of very high spinning speeds, exceeding 100kHz, have been demonstrated, and are now commercially available. In these systems, the sample diameter has to be kept small in order to limit the inertial forces. This has inevitably led to smaller and smaller samples, and the dimensions of the ro-

tors and coils of the most recent designs approach those of the micro-solenoids that were introduced for liquid-state NMR in the 1990s [46].

Solenoid micro coils have also been used for remote detection in the context of microfluidic devices. In this elegant approach, position, velocity, and in some cases, chemical information is encoded into the spin phase and polarisation inside microfluidic system, by way of a macroscopic coil which surrounds it. The fluid then flows out of the microfluidic device, and is led in a capillary through a micro coil, where the NMR signal is recorded. In this way, the velocity distribution as well as chemical reaction dynamics in microfluidic systems have been characterised in real time [47–55].

### 1.3.3

#### **Planar Detectors**

With the success of miniaturised solenoid coils, it became conceivable to integrate NMR spectroscopy with emerging microfluidic lab-on-a chip technology. Typical sample volumes in microfluidics, ranging from a few  $\mu\text{l}$  down into the  $\text{pL}$  range, are comparable to the volumes of some of the micro-solenoids that had proven superior mass sensitivity performance in hyphenated chromatography-NMR integrations. However, Lab-on-a-chip devices are typically planar, fabricated through lithographic processes, and the liquid volumes they contain are separated from each other by relatively large distances. Integrating solenoid coils into such structures, while not impossible, presents significant fabrication challenges [56]. As a possible solution, planar spiral coils were explored extensively. The first demonstration, by Stocker et al. [57], placed a sample droplet directly in contact with the micro coil. Trumbull et al. integrated a single loop inductor with a microchip-electrophoresis system [58]. The loop inductor was fabricated through a lift-off process, and the metal thickness was therefore less than  $1 \mu\text{m}$ . Since this is below the skin depth, it probably limited the sensitivity of the system. It was found that microfluidic chips made from polyimide provided considerably better spectral resolution than those made from pyrex glass, probably due to the closer match in susceptibility between the polyimide and water. While NMR spectra of test samples were successfully collected, the sensitivity of the device was not found to be sufficient for a credible integration with capillary electrophoresis.

Later implementations involved fabrication of the spiral coil structure by lift-off lithography and subsequent electroplating onto a glass microfluidic chip [59]. This allows thicker conductors, significantly reducing ohmic losses. Microfluidic probes based on this design [60] reached limits of detection of  $260 \text{ nMol} \sqrt{\text{s}}$  at  $470 \text{ nL}$  probe volume, and  $20 \text{ nMol} \sqrt{\text{s}}$  at  $30 \text{ nL}$  (values scaled to  $600 \text{ MHz}$  proton frequency). However, the spectral resolution was quite poor, insufficient to resolve homonuclear  $J$  couplings in the  $^1\text{H}$  spectra. This was probably due to the circular shape of the sample chamber that was used.

Better resolution was achieved by arranging it in a linear channel aligned with the magnetic field [61], making it possible to monitor the on-chip condensation of benzaldehyde and aniline [62]; further applications of planar spiral coil designs to

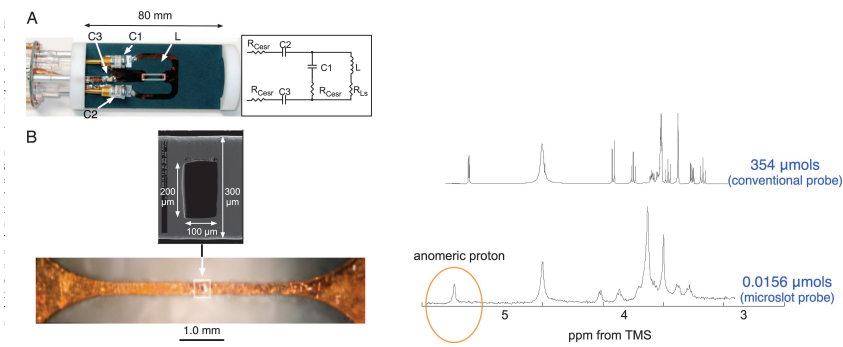


**Figure 1.4** Left: Microslot probe. A: Probe with housing removed, B: Scanning electron micrograph and light micrograph of the slotted microstrip detector. Right: Spectrum of sucrose in  $\text{H}_2\text{O}$  acquired with a conventional (top) and the slotted microstrip probe (bottom). Reprinted with permission from [71].

microfluidic reaction monitoring followed [63, 64]. Planar spiral coils have also been applied to EPR spectroscopy [65] at the micro scale.

Placing planar coils on both sides of the sample leads to the concept of micro-Helmholtz coils. These provide potentially high sensitivity and B1 homogeneity, but present considerable fabrication challenges. An elegant implementation has recently been described by Spengler et al. [66, 67]. Phased arrays provide another potential approach to planar micro-NMR detectors. A proof of concept has been given by Gruschke et al, who have demonstrated a system of 7 partially overlapping coils fabricated using a wire-bonding process [68]. This detector has been used successfully to image human skin samples [69] and to study porous media using a single-sided, permanent magnet spectrometer [70].

### 1.3.4

#### Microstrip Detectors

Given the difficulty of integrating three-dimensional coils with planar microfluidic devices, and the benefits that linear structures aligned with the B0 magnetic field offer in terms of field homogeneity, it is not surprising that microstrip detectors were considered for integrating microfluidics and NMR. A problem that arises immediately is that transmission line resonators require longitudinal dimensions that are of the order of the wavelength, which amounts to tens of centimetres for typical NMR Larmor frequencies. Maguire et al. therefore proposed slotted microstrips as a means to concentrate the RF magnetic field, and therefore the sensitivity, to a mm-sized area [71, 72]. Their design was based on a single microstrip conductor of 0.3 mm width and about 5 mm length, fabricated using RF printed circuit board material using standard wet-etching techniques (Fig. 1.4).

At the centre of this structure, a square-shaped piece of the Cu conductor was re-

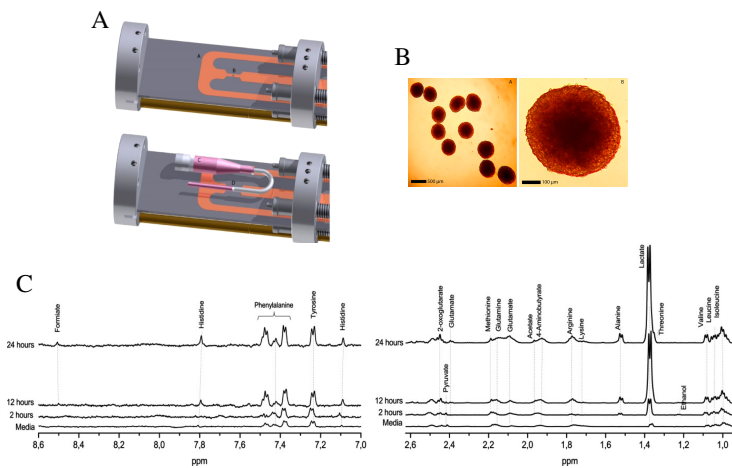


**Figure 1.5** Tumour spheroid microdevice. A: CAD rendering of the microslot probe without (top) and with (bottom) the culture device in place; B: Optical micrographs of tumour spheroids; C: 600 MHz <sup>1</sup>H NMR spectra obtained with the system. Adapted with permission from [73].

moved from the microstrip. This concentrates the current into the narrow remaining conductor bridges, and leads to a corresponding increase in local magnetic field. As a result, the mass sensitivity is significantly better than what had previously been achieved with spiral planar coils.

At the same time, a half-height line width of about 1.1 Hz was obtained, significantly superior to any other planar micro-NMR detector described up to that point. However, the baseline resolution was still relatively poor (>50 Hz at 0.5%). Nonetheless, one- and two dimensional <sup>1</sup>H NMR spectra of sucrose and of ribonuclease A were obtained successfully. Microslot probes of this type have since been applied successfully for studying the metabolism of biological systems. In one of the first credible demonstrations of microfluidic NMR metabolomics, a microslot detector was applied to obtain NMR spectra of a metabolite concentrate from a cell line by Kojanski et al [74]. More recently, the exo-metabolome of a tumour spheroid was observed directly by combining the microslot detector with an evaporation-driven perfusion micro-device [73], as shown in Fig. 1.5.

### 1.3.5 Non-Resonant Detectors

The microstrip geometry has also been used to build non-resonant NMR saddle coils [75]. In this approach, a saddle coil is defined by microstrips fabricated on a flexible printed circuit board, which is then wrapped in a cylinder to serve as a saddle-coil NMR probe. The microstrips are designed to have a specific impedance of 50Ω,

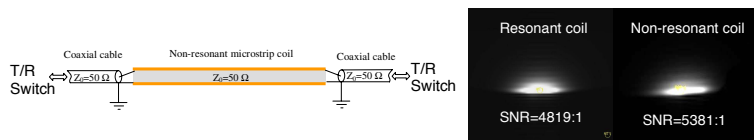


**Figure 1.6** Non-resonant microstrip detector (left), and MR images obtained from a sample of corn oil at 7 T with a resonant and a non-resonant microstrip detector. Adapted from [77].

and are terminated by a  $50\Omega$  resistor between the microstrip and ground conductors. Unlike typical NMR detectors, this system does not rely on an electromagnetic resonance (standing wave) in order to couple the detector to the transmitter/receiver system [76]. Instead, a travelling TEM wave is directly coupled to the precessing nuclear spins. The most notable advantage of this approach, commonly referred to as travelling-wave NMR, is its broad-band nature, which makes it simple to perform multinuclear NMR experiments. The saddle coil system mentioned above has been used, without re-tuning, to obtain  $^1\text{H}$ ,  $^{13}\text{C}$ ,  $^{19}\text{F}$ , and  $^{31}\text{P}$  spectra at 0.52 T. Broadband switching between transmission and receiver mode has been realised mechanically by way of a Reed relay.

Linear non resonant microstrip detectors have been investigated by Zhang et al [77], who have also performed a direct comparison of the sensitivity of a microstrip operated in non-resonant and in standing-wave mode. In a non-resonant system, the spin precession is coupled into the TEM mode of the transmission line in both directions. Therefore, Zhang et al used transmit/recieve switches at either end of the transmission line, and combined the signal power from both before pre-amplification [78]. Interestingly, the SNR from this setup was found to be the same as in the traditional standing-wave operation.

Travelling wave excitation and detection has been considered as a way to circumvent limitations of high-field full body MRI, where the dimensions of the sample are comparable to the wavelength of the RF radiation. In conventional near-field detectors, this leads to uneven phase and amplitude of the RF signals throughout the sample. Brunner et al. have demonstrated that MR images with high sensitivity and good homogeneity can be obtained at 7 T by travelling wave detection [79]. In this case, the conductive bore casing acts as a cylindrical transmission line, and the  $\text{TE}_{01}$  mode is excited using circularly polarised patch antenna near the entrance to the bore. The possibility to place the detector and excitation structures remotely from the sample is another advantage of travelling wave systems over conventional standing wave MR detectors.

Travelling wave detection has also been investigated directly in a coaxial cable running vertically through the bore of a NMR magnet, with the sample taking the place of the dielectric in the homogeneous area of the magnet [80], and a similar design using a planar transmission line has been proposed, but not yet demonstrated experimentally. A related concept has been proposed recently by Fratila et al, who

directly connected a planar micro coil between the coaxial transmission line and a matched ohmic termination [81].

### 1.3.6 Stripline Detectors

Striplines and microstrips are closely related, the main difference being that the magnetic and electric fields in a stripline are bounded on both sides by ground planes, in contrast to the one-sided microstrip. Striplines have been introduced to microwave technology earlier than microstrips, but are less commonly used in contemporary microwave circuits due to more complex fabrication. However, they do offer some advantages when used as NMR detectors.

Kentgens et al. have built a stripline detector for micro-NMR on printed circuit board, with the sample replacing the dielectric on one side of the stripline [82]. A constriction in the stripline at the location of the sample causes a concentration of the current, and correspondingly, the RF magnetic field. A PCB material with a low loss tangent was used to optimise sensitivity. The stripline was tuned and matched to both the  $^1\text{H}$  and  $^{13}\text{C}$  frequencies by inserting it as a short to ground at the end of transmission line resonators made from semirigid coaxial cable. This arrangement allows  $^1\text{H}$ - $^{13}\text{C}$  double resonance experiments; however, no such results were reported [82].

The sample volume was about 100 nL, and a mass sensitivity of  $10^{13}$  spins/ $\sqrt{\text{Hz}}$ , or about 0.1 nMol  $\sqrt{s}$  was obtained. It should be noted, however, that this refers to the single-scan detection limit, and that a more realistic measure of sensitivity would take into account the delay required for the acquisition of multiple transients. The  $B_1$  homogeneity of the detector was quite good, at a 810/90 ratio of about 60%. However, the  $B_0$  homogeneity was relatively poor in this initial design.

A more sophisticated variant was presented by Bart et al [83] (cf Fig. 1.7). The improved stripline has been designed directly as a symmetric RF resonator, supporting a  $\lambda/2$  standing wave with current nodes at the ends. A constriction at the centre of the stripline causes a local increase in magnetic field, and a concomitant increase in local sensitivity. The resonator is arranged vertically, parallel to the static magnetic field, thus minimising susceptibility broadening artefacts. The geometry of the resonator, including the constriction width, length, and angle of the taper, had been carefully optimised using finite element computations [84] for sensitivity and  $B_0$  and  $B_1$  homogeneity. Bart et al. showed that the length/width ratio of the constriction is crucial for sensitivity, and found that ratios between 5 and 10 are optimal. Steep tapers were found to be preferable in terms of sensitivity, but produce greater  $B_0$  homogeneity artefacts.

The probe was fabricated by Cu vapour deposition and subsequent electroplating onto a Si substrate, which served as a dielectric for the stripline. On one side, the sample channel is etched into the Si, replacing a part of the dielectric. Ultra pure, low-conductivity Si is an excellent insulator at room temperature, and exhibits a low loss tangent. However, it typically carries surface layer rich in defects, which lead to high dielectric and ohmic losses. To avoid these, Bart et al. deposited a layer of amorphous silicon (a-Si) before the metallisation. While this substantially in-

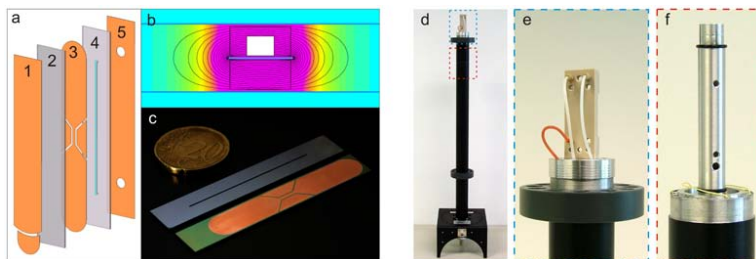


**Figure 1.7** Microfluidic NMR chip and stripline probe. (a) Conductor and dielectric layers of the stripline detector; (b) calculated RF magnetic field distribution; (c) photograph of the stripline detector and sample channel; (d-f) NMR flow probe assembly. Reprinted with permission from [85].

creased the quality of the resonator, the achieved sensitivity was still about an order of magnitude less than theoretically predicted. Nonetheless, very high quality microfluidic NMR spectra have been obtained with this system. A limit of detection of  $nLOD_{\omega} = 22.2 \text{ nMol } \sqrt{s}$  was demonstrated for the anomeric proton in sucrose in a sample volume of 600 nL, at a spectral resolution of better than 1Hz. Bart et al. also showed that a useful metabolomic spectrum could be obtained from a sample of human cerebrospinal fluid, even though this required several hours of acquisition time.

This type of stripline probe has meanwhile been adapted to a number of interesting applications. The flow-through probe described by Bart et al has been used for in-line reaction monitoring [85]. A stripline resonator similar to the first one described by van Bentum et al [86] has recently been used to obtain  $^{75}\text{As}$  NMR spectra from single crystalline epitaxially grown films of  $\text{Al}_x\text{Ga}_{(1-x)}\text{As}$ , in which 5 separate As sites could be distinguished [87].

A stripline probe has also been integrated with a electrochemical conversion assay. In order to accumulate a sufficient concentration of the electrochemical reaction products, the EC system was integrated with a solid-phase extraction column, the elute from which was then fed into the flow-through stripline NMR probe [88, 89].

An interesting recent development is the hyphenation of supercritical  $\text{CO}_2$  chromatography with NMR detection. SCF chromatography exploits the relatively low viscosity of SCF solvents, which reduce the back pressure at high flow rates compared to HPLC systems. This allows higher throughput than standard HPLC, as well as the separation of molecules that are not soluble in typical HPLC solvents. The combination of SCFC with NMR detection would be a natural fit, since the solvent does not produce an NMR signal. Also, the higher throughput means that potentially larger amounts of sample can be used and collected, which facilitates NMR observation. Finally, SCF  $\text{CO}_2$  is a very low viscosity solvent, which can have a positive impact on spectral resolution, particularly for small molecules. However, the direct in-line hyphenation of SCFC with NMR detection has not yet been reported. A proof of principle has been given by Tayler et al [90], who used an HPLC storage loop to

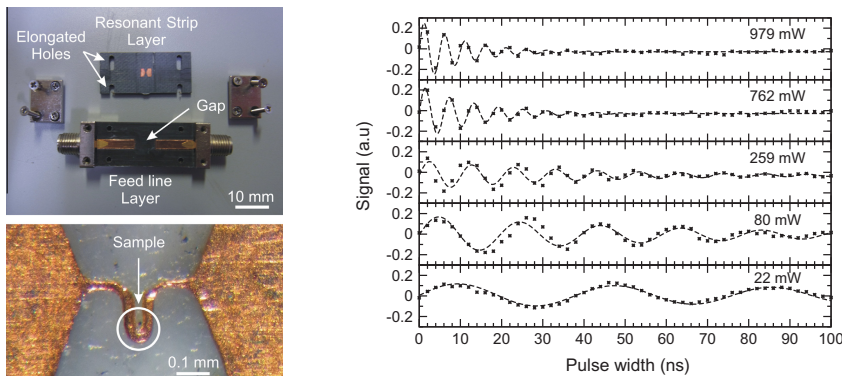


**Figure 1.8** Stripline resonator for pulsed EPR (left), and nutation diagrams obtained with this system (right). Adapted with permission from [92].

collect fractions from SCFC, which were then dissolved in methanol and injected into a stripline flow probe. Stripline and microstrip probes offer control over the detailed amplitude and phase distribution of the RF magnetic field. This opens up many possibilities to integrate spatial information into the NMR signal collection, which have only sparingly been explored to date.

Tijssen et al. showed that a tapered strip line produces a well-defined  $B_1$  gradient, and have used this in order to simultaneously acquire NMR spectra of plugs of different composition injected one after the other into the sample capillary [91]. The same system can be used for continuous-flow reaction monitoring. Tijssen et al also demonstrated that the  $B_1$  gradient generated by the tapered stripline can be used to compensate for  $B_0$  inhomogeneities, by acquiring a spatially encoded signal from which the high-resolution NMR spectrum can be retrieved by data processing. This possibility may have important applications in permanent magnet NMR systems.

Finally, it should be noted that the stripline design is not only of interest in NMR spectroscopy, but also in electron paramagnetic resonance. Yap et al. have recently described a pulsed Ku-band (17 GHz) EPR system based on a micro-stripline resonator (Fig. 1.8). In their design, several variants of the tapered stripline resonator were explored, including one where the sensitive area is formed by a narrow, U-shaped turn in the stripline conductor. Using this resonator, very high sensitivity and Rabi (nutation) frequencies in excess of 210 MHz have been obtained.

Klotz et al. have used a co-planar stripline pair to manipulate single electron spins trapped in quantum dots [93]. This type of magnetometer, as well as related systems based on NV-centre defects in diamond, could become important as highly sensitive NMR detectors in the future. Waveguide structures have also been used extensively in the design of probes for dynamic nuclear polarisation, which require simultaneous irradiation at NMR and EPR frequencies (see below).

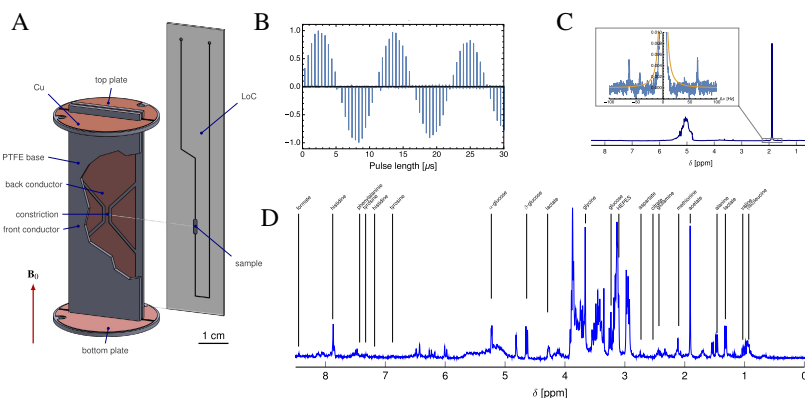


**Figure 1.9** PTL resonator for microfluidic NMR. A: CAD rendering of the resonator and the lab-on-a-chip device; B: experimental nutation curve at 10 W; C: 150 mM acetate in H<sub>2</sub>O spectrum demonstrating excellent baseline resolution; D: <sup>1</sup>H spectrum of 2 μl of cell growth medium containing 20 mM glucose, and less than 1 mM concentrations of various amino acids. The spectrum was acquired in about 20 min. Adapted with permission from [94].

### 1.3.7

#### Parallel Plate Transmission Lines

Parallel plate transmission lines (PTL), comprised of two parallel conductors of equal width, share some of the characteristics of both stripline and microstrip waveguides. In particular for large  $w/h$  ratios, the electric field is largely contained in the dielectric space between the conductors. However, there is some spillover into the surrounding space, and the magnetic field lines are not contained, but loop around each conductor, as shown in Fig. 1.1D. Like microstrips, and in contrast to striplines, PTL do not support a pure TEM mode in general, due to the difference in dielectric constant between the dielectric material and the surrounding air. In the context of magnetic resonance detectors, the PTL geometry is a natural fit with planar samples, and it is somewhat surprising that it has not been exploited more extensively to date.

Jasisnksi et al have built a micro imaging NMR probe head using a resonator based on a PTL of 5 mm length and 0.3 mm width [95]. The  $w/h$  ratio had been optimised using two-dimensional finite element calculations; it was found that  $w/h$  values in the vicinity of unity provided a good compromise between RF homogeneity, filling factor, and sensitivity. The PTL was tuned and matched to a 50 Ohm coaxial cable, giving an unloaded Q factor of 120, in good agreement with the finite element simulations. The resonator was placed in a magnetic field of 11.7 T, with the magnetic field direction normal to the conductor planes. High quality images of 24 × 24 × 300 μm resolution on 128 × 128 points could be obtained in about 45 minutes.

A similar detector was built by Finch et al [94] for microfluidic NMR spectroscopy. Their geometry was an adaptation of the stripline probe proposed by Bart et al. [83],

consisting of a half-wave resonator with the waveguide axis parallel to the magnetic field, and a constriction at the location of the sample (cf. Fig. 1.9). Unlike earlier microfluidic NMR probes, which used fixed capillaries requiring fluidic sample connections, the probe by Finch et al was designed to accommodate a wide range of lab-on-a-chip devices manufactured from PMMA sheet material by either by hot embossing, or by inexpensive rapid prototyping techniques based on a digital laser cutting system.

Starting from a requirement of a sample chamber volume of 2  $\mu\text{l}$ , Finch et al. used a numerical search algorithm in combination with a 3D finite element model of the resonator to optimise simultaneously the probe chamber dimensions (width  $\times$  length), and the corresponding dimensions of the constriction in the resonator. The optimisation was balanced between the conflicting targets of high sensitivity and RF homogeneity, resulting in a compromise design. This probe achieved a frequency-domain limit of detection of  $\text{nLOD}_\omega = 1.57 \text{ nMol}\sqrt{\text{s}}$  (based on signal averaging over multiple transients), at a line width of 1.78 Hz (at 7 T). Importantly, the line widths at 0.5% and 0.1% height were inside of a Lorentzian line with the same half-width (Fig. 1.9C). This baseline resolution is of particular importance in metabolomic studies [96, 97], where signals of widely differing intensity appear, and broad feet from strong lines can obscure weaker signals.

### 1.3.8

#### **Applications in Solid State Physics**

Planar waveguide structures have been used extensively in solid state physics, including in experiments that relate directly or indirectly to magnetic resonance. For example, Yusa et al. have demonstrated the detection of nuclear spin states in GaAs by subtle effects of the nuclear magnetism on the conduction of photo-induced charge carriers [98] (cf also [99]). This allowed the detection of as few as  $10^8$  nuclear spins, which is a remarkable achievement even at the experimental temperature of 100 mK.

Conducting microstrips have been deposited on top of a ferromagnetic layers in order to obtain broadband ferromagnetic resonance signals. In this way, the magnetic properties of thin film structures can be studied by inductive microwave spectroscopy [100, 101]. Similar techniques using optical detection have been described, as well [102].

### 1.3.9

#### **Waveguides for Dynamic Nuclear Polarisation**

While optimised detector geometries mitigate the inherently poor sensitivity of the NMR experiment, they do not ultimately address its root cause: the magnetic polarisation of nuclear spins is minuscule (of the order of 1 spin in  $10^5$ ), even at the highest practical magnetic fields. Sample cooling helps to an extent, but is undesirable for many systems, in particular in biology.

Several methods are known to temporarily increase the nuclear polarisation above the thermodynamic equilibrium value, including parahydrogen-induced polarisation,

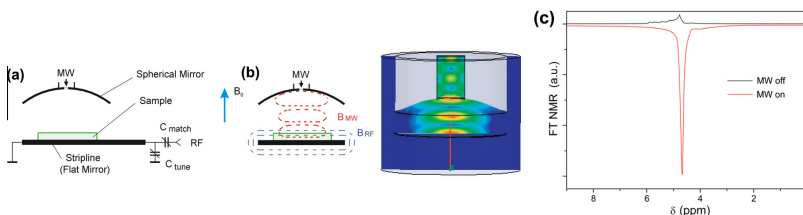


**Figure 1.10** Liquid-state DNP system based on a Fabry-Perot microwave resonator combined with a stripline RF resonator. Adapted with permission from [106].

optical pumping, and dynamic nuclear polarisation (DNP). Each of these has its merits and limitations. Among them, DNP is of most interest in the present context, because it places special requirements on the resonator structure surrounding the sample.

DNP transfers polarisation from the electron to the nuclear spins by cross-relaxation. A radical species needs to be present in the sample, with suitable electron spin relaxation times to make the transfer feasible. Stable nitroxide radicals are commonly used for this purpose. DNP requires saturation, or at least significant perturbation, of the electron spin temperature by microwave irradiation. At typical NMR magnetic fields, this involves microwave frequencies up to several hundred GHz. Transporting microwave power in this part of the spectrum requires carefully designed waveguide structures. DNP tends to be most efficient in the solid state, and at cryogenic temperatures.

This has led to the development of dissolution-DNP techniques [103], in which the sample is first irradiated with microwaves at liquid He temperature or somewhat below for about an hour or so, then rapidly dissolved in a hot solvent, to be transferred to an NMR magnet for spectroscopy, or injected into a live subject inside an MRI scanner for imaging [104].

The dissolution DNP technique does not lend itself to small scale applications, due to the experimental overhead; relatively large (ml) volumes of hyperpolarised materials are produced in a batch process, with polarisation life times of only a few minutes at best.

At small enough scale, it is possible to avoid the dissolution and the transfer step, and rapidly melt the sample in-situ after microwave irradiation by means of either an electric heater or exposure to a hot gas. This has been achieved recently by Sharma et al. [105]. A capillary of  $360\text{ }\mu\text{m}$  outer diameter is moved between three regions inside an NMR magnet: a cold region at 77 K, where the sample is irradiated with microwaves, a hot region, where the capillary is exposed to a stream of warm nitrogen gas, and an NMR region, where the NMR spectrum is measured using a stripline resonator.

DNP also works directly in the liquid state. However, the transfer tends to lose efficiency at high magnetic fields, and the penetration depth of microwaves at high

frequency into most liquids at ambient temperature is very poor. Nonetheless, there is considerable interest in direct liquid-state DNP [107–109] due to its conceptual simplicity, and because it could potentially be applied to systems that cannot tolerate freezing and thawing. Liquid-state DNP systems are essentially electron-nuclear double resonance spectrometers, and require irradiation at both the nuclear and electron Larmor frequencies simultaneously or at least in short succession. The design of suitable resonators is challenging, since the low-frequency structure tends to shield the sample from access to the high-frequency radiation.

Annino et al [110–112] have designed a dielectric cavity microwave resonator combined with a waveguide radio frequency resonator based on a pair of straight wires, operating at a magnetic field of 3.3T. This corresponds to electron and proton Larmor frequencies of 95 GHz and 150 MHz, respectively. The microwave power is coupled in through a rectangular waveguide from a solid state source. At a microwave power of about 70 mW, an enhancement of the proton signal of -16 was observed in mixture of dioxane and water containing a nitroxide radical.

Another design has recently been presented by Denysenkov et al. [106, 113–115] Their system operates at even higher frequencies, with a magnetic field of 9.2 T (392 MHz NMR / 260 GHz EPR frequencies). They employ a much more powerful gyrotron microwave source, which is coupled into the DNP system using a corrugated waveguide. The microwaves emanate from the waveguide into a Fabry-Perot resonator, the back (mirror) plane of which is formed by a stripline radio frequency resonator, as shown in Fig. 1.10.

The sample forms a thin liquid film of  $20 \mu\text{m}$  thickness and  $50 \text{ nl}$  volume directly on the conducting stripline surface. This ensures excellent thermal contact, and prevents the liquid from heating up too much upon microwave irradiation. The microwave power employed in Denysenkov's design is about two orders of magnitude stronger than in the one by Annino et al. Signal enhancements of up to a factor of 30 have been observed with this system.



## References

- 1 Abragam, A. (1961) *The Principles of Nuclear Magnetism*, Oxford University Press.
- 2 Rabi, I., Zacharias, J., Millman, S., and Kusch, P. (1938) A new method of measuring nuclear magnetic moment. *Physical Review*, **53** (4), 318–318.
- 3 Bloch, F. (1946) Nuclear Induction. *Phys. Rev.*, **70** (7-8), 460–474.
- 4 Purcell, E.M., Torrey, H.C., and Pound, R.V. (1946) Resonance Absorption by Nuclear Magnetic Moments in a Solid. *Phys. Rev.*, **69** (1-2), 37–38.
- 5 Ernst, R.R. and Anderson, W.A. (1966) Application of Fourier Transform Spectroscopy to Magnetic Resonance. *Review of Scientific Instruments*, **37** (1), 93–102.
- 6 Bechinger, B. and Opella, S.J. (1991) Flat-coil probe for NMR spectroscopy of oriented membrane samples. *Journal of Magnetic Resonance* (1969), **95** (3), 585–588.
- 7 Zhang, X., Ugurbil, K., and Chen, W. (2001) Microstrip RF surface coil design for extremely high-field MRI and spectroscopy. *Magn. Reson. Med.*, **46** (3), 443–450.
- 8 Hoult, D. and Richards, R. (1975) Critical Factors in the Design of Sensitive High Resolution Nuclear Magnetic Resonance Spectrometers. *Proceedings of the Royal Society of London. Series A, Mathematical and Physical Sciences*, **344** (1638), 311–340.
- 9 Webb, A. (2005) Nuclear magnetic resonance coupled microseparations. *Magn Reson Chem*, **43**, 688–696.
- 10 Manz, A., Graber, N., and WIDMER, H. (1990) Miniaturized Total Chemical-Analysis Systems - a Novel Concept for Chemical Sensing. *Sensor Actuat B-Chem*, **1**, 244–248.
- 11 Pozar, D. (2012) *Microwave Engineering*, John Wiley & Sons, 4th edn..
- 12 Barret, R.M. (1955) Microwave Printed Circuits - A Historical Survey. *Microwave Theory and Techniques, IRE Transactions on*, **3** (2), 1–9.
- 13 Hoult, D.I. and Richards, R.E. (1976) The signal-to-noise ratio of the nuclear magnetic resonance experiment. *Journal of Magnetic Resonance* (1969), **24** (1), 71–85.
- 14 Bridges, J.F. and Advanced Nmr Systems, Inc. (1988), Cavity resonator with improved magnetic field uniformity for high frequency operation and reduced dielectric heating in NMR imaging devices, US Patent Office.
- 15 Bogdanov, G. and Ludwig, R. (2002) Coupled microstrip line transverse electromagnetic resonator model for high-field magnetic resonance imaging. *Magn. Reson. Med.*, **47** (3), 579–593.
- 16 Hayes, C.E., Edelstein, W.A., Schenck, J.F., Mueller, O.M., and Eash, M. (1985) An efficient, highly homogeneous radiofrequency coil for whole-body NMR imaging at 1.5 T. *J. Magn. Reson*, **63**, 622–628.
- 17 Zhang, X., Ugurbil, K., Chen, W., and Regents Of The University Of Minnesota (2006), Method and apparatus for magnetic resonance imaging and spectroscopy using microstrip transmission line coils, US Patent Office.
- 18 Zhang, X., Zhu, X.H., and Chen, W.

- (2005) Higher-order harmonic transmission-line RF coil design for MR applications. *Magn. Reson. Med.*, **53** (5), 1234–1239.
- 19** Burian, M. and Hjek, M. (2004) Linear microstrip surface coil for MR imaging of the rat spinal cord at 4.7 T. *Magn Reson Mater Phy*, **17** (3-6), 359–362.
- 20** Zhang, X., Ugurbil, K., and Chen, W. (2003) A microstrip transmission line volume coil for human head MR imaging at 4T. *Journal of Magnetic Resonance*, **161** (2), 242–251.
- 21** Driesel, W., Mildner, T., and Möller, H.E. (2008) A microstrip helmet coil for human brain imaging at high magnetic fields. *Concepts in Magnetic Resonance Part B: Magnetic Resonance Engineering*, **33B** (2), 94–108.
- 22** Vaughan, J.T., Adriany, G., Garwood, M., Yacoub, E., Duong, T., DelaBarre, L., Andersen, P., and Ugurbil, K. (2002) Detunable transverse electromagnetic (TEM) volume coil for high-field NMR. *Magn. Reson. Med.*, **47** (5), 990–1000.
- 23** Lee, R.F., Westgate, C.R., Weiss, R.G., Newman, D.C., and Bottomley, P.A. (2001) Planar strip array (PSA) for MRI. *Magn. Reson. Med.*, **45** (4), 673–683.
- 24** Boskamp, E.B., Lee, R.F., and Ge Medical Systems Global Technology Company, L. (2006) Multiple channel, microstrip transceiver volume array for magnetic resonance imaging, US Patent Office.
- 25** Roemer, P.B., Edelstein, W.A., Hayes, C.E., Souza, S.P., and Mueller, O.M. (1990) The NMR phased array. *Magn. Reson. Med.*, **16** (2), 192–225.
- 26** Hoult, D., Kolansky, G., Kripiakevich, D., and King, S. (2004) The NMR multi-transmit phased array: a Cartesian feedback approach. *J. Magn. Reson.*, **171** (1), 64–70.
- 27** van den Bergen, B., Klomp, D.W.J., Raaijmakers, A.J.E., de Castro, C.A., Boer, V.O., Kroese, H., Luijten, P.R., Lagendijk, J.J.W., and van den Berg, C.A.T. (2010) Uniform prostate imaging and spectroscopy at 7 T: comparison between a microstrip array and an endorectal coil. *NMR in Biomedicine*, **24**, 358–365.
- 28** Adriany, G., Van de Moortele, P.F., Wiesinger, F., Moeller, S., Strupp, J.P., Andersen, P., Snyder, C., Zhang, X., Chen, W., Pruessmann, K.P., Boesiger, P., Vaughan, T., and Ugurbil, K. (2005) Transmit and receive transmission line arrays for 7 Tesla parallel imaging. *Magn. Reson. Med.*, **53** (2), 434–445.
- 29** Wu, B., Zhang, X., Qu, P., and Shen, G.X. (2006) Design of an inductively decoupled microstrip array at 9.4T. *Journal of Magnetic Resonance*, **182** (1), 126–132.
- 30** Wang, C. and Shen, G.X. (2006) B1 field, SAR, and SNR comparisons for birdcage, TEM, and microstrip coils at 7T. *Journal of Magnetic Resonance Imaging*, **24** (2), 439–443.
- 31** van den Bergen, B., van den Berg, C.A.T., Klomp, D.W.J., and Lagendijk, J.J.W. (2009) SAR and power implications of different RF shimming strategies in the pelvis for 7T MRI. *Journal of Magnetic Resonance Imaging*, **30** (1), 194–202.
- 32** Ipek, Ö., Raaijmakers, A.J.E., Klomp, D.W.J., Lagendijk, J.J.W., Luijten, P.R., and van den Berg, C.A.T. (2012) Characterization of transceive surface element designs for 7 tesla magnetic resonance imaging of the prostate: radiative antenna and microstrip. *Phys. Med. Biol.*, **57** (2), 343–355.
- 33** Olson, D., Peck, T., Webb, A., Magin, R., and Sweedler, J. (1995) High-Resolution Microcoil  $^1\text{H}$ -NMR for Mass-Limited, Nanoliter-Volume Samples. *Science*, **270** (5244), 1967–1970.
- 34** Sweedler, J.V., Peck, T.L., Webb, A.G., Magin, R.L., Wu, N., and The Board Of Trustees Of The University Of Illinois (1997) Method and apparatus for NMR spectroscopy of nanoliter volume samples, US Patent Office.
- 35** Lacey, M.E., Subramanian, R., Olson, D., Webb, A., and Sweedler, J. (1999) High-resolution NMR spectroscopy of sample volumes from 1 nL to 10 mu L. *Chem. Rev.*, **99** (10), 3133–3152.
- 36** Peck, T., Webb, A., Wu, N., Magin, R., and Sweedler, J. (1994) On-line NMR detection in capillary electrophoresis using an RF microcoil, in *IEMBS-94*, IEEE, pp. 986–987 vol.2.
- 37** Wu, N., Peck, T.L., Webb, A.G., Magin,

- R.L., and Sweedler, J.V. (1994) Nanoliter Volume Sample cells for  $^1\text{H}$  NMR: Application to Online Detection in Capillary Electrophoresis. *J. Am. Chem. Soc.*, **116** (17), 7929–7930.
- 38** Olson, D., Lacey, M.E., Webb, A., and Sweedler, J. (1999) Nanoliter-volume  $H\text{-}1$  NMR detection using periodic stopped-flow capillary electrophoresis. *Analytical chemistry*, **71** (15), 3070–3076.
- 39** Lacey, M.E., Tan, Z.J., Webb, A.G., and Sweedler, J.V. (2001) Union of capillary high-performance liquid chromatography and microcoil nuclear magnetic resonance spectroscopy applied to the separation and identification of terpenoids. *Journal of Chromatography A*, **922** (1-2), 139–149.
- 40** Seeber, D.A., Hoftiezer, J.H., Daniel, W.B., Rutgers, M.A., and Pennington, C.H. (2000) Triaxial magnetic field gradient system for microcoil magnetic resonance imaging. *Review of Scientific Instruments*, **71** (11), 4263–4272.
- 41** Ciobanu, L., Seeber, D.A., and Pennington, C.H. (2002) 3D MR microscopy with resolution  $3.7 \mu\text{m}$  by  $3.3 \mu\text{m}$  by  $3.3 \mu\text{m}$ . *Journal of Magnetic Resonance*, **158** (1-2), 178–182.
- 42** K Yamauchi, Imada, T., and Asakura, T. (2005) Use of Microcoil Probehead for Determination of the Structure of Oriented Silk Fibers by Solid-State NMR. *J. Phys. Chem. B*, **109** (37), 17 689–17 692.
- 43** Kentgens, A.P.M., Bart, J., van Bentum, P.J.M., Brinkmann, A., van Eck, E., Gardeniers, J.G.E., Janssen, J.W.G., Knijn, P., Vasa, S., and Verkuijlen, M.H.W. (2008) High-resolution liquid- and solid-state nuclear magnetic resonance of nanoliter sample volumes using microcoil detectors. *J Chem Phys*, **128** (5), 052 202.
- 44** Sakellariou, D., Goff, G.L., and Jacquinet, J.F. (2007) High-resolution, high-sensitivity NMR of nanolitre anisotropic samples by coil spinning. *Nature*, **447** (7145), 694–697.
- 45** Jacquinet, J.F. and Sakellariou, D. (2011) NMR Signal Detection using Inductive Coupling: Applications to Rotating Microcoils. *Concepts in Magnetic Resonance Part A*, **38A** (2), 33–51.
- 46** Samoson, A., Tuherm, T., Past, J., Reinhold, A., Heinmaa, I., Anupöld, T., Smith, M.E., and Pike, K.J. (2010) *Fast Magic-Angle Spinning: Implications*, John Wiley & Sons, Ltd, Chichester, UK.
- 47** Hilty, C., McDonnell, E., Granwehr, J., Pierce, K., Han, S., and Pines, A. (2005) Microfluidic gas-flow profiling using remote-detection NMR. *P Natl Acad Sci Usa*, **102** (42), 14 960–14 963.
- 48** McDonnell, E., Han, S., Hilty, C., Pierce, K., and Pines, A. (2005) NMR analysis on microfluidic devices by remote detection. *Anal. Chem.*, **77** (24), 8109–8114.
- 49** Harel, E., Hilty, C., Koen, K., McDonnell, E.E., and Pines, A. (2007) Time-of-flight flow imaging of two-component flow inside a microfluidic chip. *Phys Rev Lett*, **98** (1), 017 601.
- 50** Bouchard, L.S., Burt, S.R., Anwar, M.S., Kovtunov, K.V., Koptyug, I.V., and Pines, A. (2008) NMR Imaging of Catalytic Hydrogenation in Microreactors with the Use of para-Hydrogen. *Science*, **319** (5862), 442–445.
- 51** Ledbetter, M.P., Savukov, I.M., Budker, D., Shah, V., Knappe, S., Kitching, J., Michalak, D.J., Xu, S., and Pines, A. (2008) Zero-field remote detection of NMR with a microfabricated atomic magnetometer. *Proc. Natl. Acad. Sci. USA*, **105** (7), 2286–2290.
- 52** Harel, E. (2009) Magnetic resonance detection: spectroscopy and imaging of lab-on-a-chip. *Lab Chip*, **9** (1), 17–23.
- 53** Bajaj, V.S., Paulsen, J., Harel, E., and Pines, A. (2010) Zooming In on Microscopic Flow by Remotely Detected MRI. *Science*, **330** (6007), 1078–1081.
- 54** Telkki, V.V. and Zhivonitko, V.V. (2011) Analysis of remote detection travel time curves measured from microfluidic channels. *J. Magn. Reson*, **210** (2), 238–245.
- 55** Telkki, V.V., Zhivonitko, V.V., Selent, A., Scotti, G., Leppäniemi, J., Franssila, S., and Koptyug, I.V. (2014) Lab-on-a-Chip Reactor Imaging with Unprecedented Chemical Resolution by Hadamard-Encoded Remote Detection NMR. *Angew. Chem.*, **126** (42), 11 471–11 475.
- 56** Badilita, V., Kratt, K., Baxan, N.,

- Mohmmadzadeh, M., Burger, T., Weber, H., von Elverfeldt, D., Hennig, J., Korvink, J.G., and Wallrabe, U. (2010) On-chip three dimensional microcoils for MRI at the microscale. *Lab Chip*, **10** (11), 1387–1390.
- 57** Stocker, J.E., Peck, T., Webb, A., Feng, M., and Magin, R. (1997) Nanoliter volume, high-resolution NMR microspectroscopy using a 60- $\mu\text{m}$  planar microcoil. *IEEE Transactions on Biomedical Engineering*, **44** (11), 1122–1127.
- 58** Trumbull, J.D., Glasgow, I.K., Beebe, D.J., and Magin, R. (2000) Integrating microfabricated fluidic systems and NMR spectroscopy. *IEEE Transactions on Biomedical Engineering*, **47** (1), 3–7.
- 59** Massin, C., Boero, G., Vincent, F., Abenham, J., Besse, P., and Popovic, R.S. (2002) High-Q factor RF planar microcoils for micro-scale NMR spectroscopy. *Sensors & Actuators: A. Physical*, **97-98**, 280–288.
- 60** Massin, C., Vincent, F., Homsy, A., Ehrmann, K., Boero, G., Besse, P., Daridon, A., Verpoorte, E., de Rooij, N., and Popovic, R. (2003) Planar microcoil-based microfluidic NMR probes. *Journal of Magnetic Resonance*, **164** (2), 242–255.
- 61** Wensink, H., Hermes, D.C., and van den Berg, A. (2004) High signal to noise ratio in low field NMR on chip, simulations and experimental results, in *MEMSYS-04*, IEEE, pp. 407–410.
- 62** Wensink, H., Benito-Lopez, F., Hermes, D.C., Verboom, W., Gardeniers, H.J.G.E., Reinhoudt, D.N., and van den Berg, A. (2005) Measuring reaction kinetics in a lab-on-a-chip by microcoil NMR. *Lab Chip*, **5** (3), 280–284.
- 63** Gomez, M.V., Verputten, H.H.J., Diaz-Ortiz, A., Moreno, A., de la Hoz, A., and Velders, A.H. (2010) On-line monitoring of a microwave-assisted chemical reaction by nanolitre NMR-spectroscopy. *Chem. Commun.*, **46** (25), 4514.
- 64** Yue, J., Schouten, J.C., and Nijhuis, T.A. (2012) Integration of Microreactors with Spectroscopic Detection for Online Reaction Monitoring and Catalyst Characterization. *Ind. Eng. Chem. Res.*, **51** (45), 14 583–14 609.
- 65** Boero, G., Bouterfas, M., Massin, C., Vincent, F., Besse, P., Popovic, R.S., and Schweiger, A. (2003) Electron-spin resonance probe based on a 100  $\mu\text{m}$  planar microcoil. *Review of Scientific Instruments*, **74** (11), 4794–4798.
- 66** Spengler, N., Moazenzadeh, A., Meier, R.C., Badilita, V., Korvink, J.G., and Wallrabe, U. (2014) Micro-fabricated Helmholtz coil featuring disposable microfluidic sample inserts for applications in nuclear magnetic resonance. *J. Micromech. Microeng.*, **24** (3), 034 004.
- 67** Spengler, N., Höfflin, J., Moazenzadeh, A., Mager, D., MacKinnon, N., Badilita, V., Wallrabe, U., and Korvink, J.G. (2016) Heteronuclear Micro-Helmholtz Coil Facilitates  $\mu\text{m}$ -Range Spatial and Sub-Hz Spectral Resolution NMR of nL-Volume Samples on Customisable Microfluidic Chips. *Plos One*, **11** (1), e0146 384.
- 68** Gruschke, O.G., Baxan, N., Clad, L., Kratt, K., von Elverfeldt, D., Peter, A., Hennig, J., Badilita, V., Wallrabe, U., and Korvink, J.G. (2012) Lab on a chip phased array MR multi-platform analysis system. *Lab Chip*, **12** (3), 495–502.
- 69** Göbel, K., Gruschke, O.G., and Leupold, J. (2014) Phased array of microcoils allows MR microscopy of ex vivo human skin samples at 9.4 T. *Skin Res. Techn.*, **0**, 1–8.
- 70** Oligschläger, D., Lehmkühl, S., Watzlaw, J., Binders, S., de Boever, E., Rehorn, C., Vossel, M., Schnakenberg, U., and Blümich, B. (2015) Miniaturized multi-coil arrays for functional planar imaging with a single-sided NMR sensor. *Journal of Magnetic Resonance*, **254**, 10–18.
- 71** Maguire, Y., Chuang, I., Zhang, S., and Gershenfeld, N. (2007) Ultra-small-sample molecular structure detection using microslot waveguide nuclear spin resonance. *Proc. Natl. Acad. Sci. USA*, **104** (22), 9198–9203.
- 72** Maguire, Y., Gershenfeld, N., and Chuang, I.L. (2009) Slitted and stubbed microstrips for high sensitivity, near-field electromagnetic detection of small

- samples and fields, US Patent Office.
- 73** Kalfe, A., Telfah, A., Lambert, J., and Hergenröder, R. (2015) Looking into Living Cell Systems: Planar Waveguide Microfluidic NMR Detector for in Vitro Metabolomics of Tumor Spheroids. *Analytical chemistry*, **87** (14), 7402–7410.
- 74** Krajanski, H., Lambert, J., Gerikalan, Y., Suter, D., and Hergenröder, R. (2008) Microslot NMR probe for metabolomics studies. *Anal. Chem.*, **80** (22), 8668.
- 75** Murphree, D., Cahn, S.B., Rahmlow, D., and DeMille, D. (2007) An easily constructed, tuning free, ultra-broadband probe for NMR. *Journal of Magnetic Resonance*, **188** (1), 160–167.
- 76** Mispelter, J., Lupu, M., and Briguet, A. (2006) *NMR Probeheads for Biophysical and Biomedical Experiments, Theoretical Principles & Practical Guidelines*, Imperial College Press.
- 77** Zhang, X., Wang, C., Xie, Z., and Wu, B. (2008) Non-resonant microstrip (NORM) RF coils: an unconventional RF solution to MR imaging and spectroscopy, in *Proc. Intl. Soc. Mag. Reson. Med.*, p. 435.
- 78** Zhang, X., Wang, C., and Vigneron, D. (2009) Studies on MR Reception Efficiency and SNR of Non-resonance RF Method (NORM). *Proc. Intl. Soc. Mag. Reson. Med.*, p. 104.
- 79** Brunner, D.O., De Zanche, N., Fröhlich, J., Paska, J., and Pruessmann, K.P. (2009) Travelling-wave nuclear magnetic resonance. *Nature*, **457** (7232), 994–998.
- 80** Tang, J.A., Wiggins, G.C., Sodickson, D.K., and Jerschow, A. (2011) Cutoff-free traveling wave NMR. *Concepts in Magnetic Resonance Part A*, **38A** (5), 253–267.
- 81** Fratila, R.M., Gomez, M.V., Sýkora, S., and Velders, A.H. (2014) Multinuclear nanoliter one-dimensional and two-dimensional NMR spectroscopy with a single non-resonant microcoil. *Nature Communications*, **5**, 1–8.
- 82** van Bentum, P.J.M., Janssen, J.W.G., Kentgens, A.P.M., Bart, J., and Gardeniers, J.G.E. (2007) Stripline probes for nuclear magnetic resonance. *J. Magn. Reson.*, **189** (1), 104–113.
- 83** Bart, J., Kolkman, A.J., Oosthoek-de Vries, A.J., Koch, K., Nieuwland, P.J., Janssen, H.J.W.G., van Bentum, P.J.M., Ampt, K.A.M., Rutjes, F.P.J.T., Wijmenga, S.S., Gardeniers, H.J.G.E., and Kentgens, A.P.M. (2009) A Microfluidic High-Resolution NMR Flow Probe. *J Am Chem Soc*, **131** (14), 5014–5015.
- 84** Bart, J., Janssen, J.W.G., van Bentum, P.J.M., Kentgens, A.P.M., and Gardeniers, J.G.E. (2009) Optimization of stripline-based microfluidic chips for high-resolution NMR. *J. Magn. Reson.*, **201** (2), 175–185.
- 85** Bart, J., Oosthoek-de Vries, A.J., Tijssen, K.C.H., Janssen, J.W.G., Bentum, P.J.M., Gardeniers, J., and Kentgens, A. (2010) In-line NMR analysis using stripline based detectors, in *MicroTAS*, pp. 2086–2088.
- 86** van Bentum, P.J.M. and Kentgens, A.P.M. (2008) High-Sensitivity NMR Probe Systems, in *Modern Magnetic Resonance*, Springer Netherlands, Dordrecht, pp. 353–361.
- 87** Goswami, M., Knijn, P.J., Bauhuis, G.J., Janssen, J.W.G., van Bentum, P.J.M., de Wijs, G.A., and Kentgens, A.P.M. (2014) Stripline 75As NMR Study of Epitaxial III-V Semiconductor Al<sub>0.5</sub>Ga<sub>0.5</sub>As. *J. Phys. Chem. C*, **118** (25), 13 394–13 405.
- 88** Falck, D., Vries, A.J.O.d., Kolkman, A., Lingeman, H., Honing, M., Wijmenga, S.S., Kentgens, A.P.M., and Niessen, W.M.A. (2013) EC-SPE-stripline-NMR analysis of reactive products: a feasibility study. *Analytical and Bioanalytical Chemistry*, **405** (21), 6711–6720.
- 89** Falck, D. and Niessen, W.M.A. (2015) Solution-phase electrochemistry-nuclear magnetic resonance of small organic molecules. *TrAC Trends in Analytical Chemistry*, **70**, 31–39.
- 90** Tayler, M.C.D., van Meerten, S.B.G.J., Kentgens, A.P.M., and van Bentum, P.J.M. (2015) Analysis of mass-limited mixtures using supercritical-fluid chromatography and microcoil NMR. *Analyst*, **140** (18), 6217–6221.
- 91** Tijssen, K.C.H., Bart, J., Tiggelaar, R.M., Janssen, J.W.G.H., Kentgens, A.P.M., and van Bentum, P.J.M. (2016) Spatially resolved spectroscopy using tapered stripline NMR. *Journal of Magnetic Resonance*, **263**, 136–146.

- 92** Yap, Y.S., Yamamoto, H., Tabuchi, Y., Negoro, M., Kagawa, A., and Kitagawa, M. (2013) Strongly driven electron spins using a Ku band stripline electron paramagnetic resonance resonator. *Journal of Magnetic Resonance*, **232**, 62–67.
- 93** Klotz, F., Huebl, H., Heiss, D., Klein, K., Finley, J.J., and Brandt, M.S. (2011) Coplanar stripline antenna design for optically detected magnetic resonance on semiconductor quantum dots. *Rev. Sci. Instrum.*, **82** (7), 074707.
- 94** Finch, G., Yilmaz, A., and Utz, M. (2016) An optimised detector for in-situ high-resolution NMR in microfluidic devices. *Journal of Magnetic Resonance*, **262**, 73–80.
- 95** Jasinski, K., Mlynarczyk, A., Latta, P., Volotovskyy, V., Węglarz, W.P., and Tomanek, B. (2012) A volume microstrip RF coil for MRI microscopy. *Magn Reson Imaging*, **30** (1), 70–77.
- 96** Pan, Z. and Raftery, D. (2007) Comparing and combining NMR spectroscopy and mass spectrometry in metabolomics. *Analytical and Bioanalytical Chemistry*, **387** (2), 525–527.
- 97** Zhang, S., Gowda, G.A.N., Ye, T., and Raftery, D. (2010) Advances in NMR -based biofluid analysis and metabolite profiling. *Analyst*, **135** (7), 1490–1498.
- 98** Yusa, G., Muraki, K., Takashina, K., Hashimoto, K., and Hirayama, Y. (2005) Controlled multiple quantum coherences of nuclear spins in a nanometre-scale device. *Nature*, **434** (7036), 1001–1005.
- 99** Tycko, R. (2005) Techniques: NMR on a chip. *Nature*, **434** (7036), 966–967.
- 100** Kostylev, M. (2009) Strong asymmetry of microwave absorption by bilayer conducting ferromagnetic films in the microstrip-line based broadband ferromagnetic resonance. *Journal of Applied Physics*, **106** (4), 043903.
- 101** Kostylev, M., Stashkevich, A.A., Adeyeye, A.O., Shakespeare, C., Kostylev, N., Ross, N., Kennewell, K., Magaraggia, R., Roussigné, Y., and Stamps, R.L. (2010) Magnetization pinning in conducting films demonstrated using broadband ferromagnetic resonance. *Journal of Applied Physics*, **108** (10), 103914.
- 102** Keatley, P.S., Kruglyak, V.V., Barman, A., Ladak, S., Hicken, R.J., Scott, J., and Rahman, M. (2005) Use of microscale coplanar striplines with indium tin oxide windows in optical ferromagnetic resonance measurements. *Journal of Applied Physics*, **97** (10).
- 103** Ardenkjær-Larsen, J.H. (2016) On the present and future of dissolution-DNP. *Journal of Magnetic Resonance*, **264**, 3–12.
- 104** Brindle, K.M., Bohndiek, S.E., Gallagher, F.A., and Kettunen, M.I. (2011) Tumor imaging using hyperpolarized <sup>13</sup>C magnetic resonance spectroscopy. *Magn. Reson. Med.*, **66** (2), 505–519.
- 105** Sharma, M., Janssen, G., Leggett, J., Kentgens, A.P.M., and van Bentum, P.J.M. (2015) Rapid-melt Dynamic Nuclear Polarization. *Journal of Magnetic Resonance*, **258**, 40–48.
- 106** Denysenkov, V. and Prisner, T. (2012) Liquid state Dynamic Nuclear Polarization probe with Fabry–Perot resonator at 9.2T. *Journal of Magnetic Resonance*, **217**, 1–5.
- 107** Loening, N.M., Rosay, M., Weis, V., and al, e. (2002) Solution-state dynamic nuclear polarization at high magnetic field. *Journal of the American ...*, **124**, 8808–8809.
- 108** Lingwood, M.D. and Han, S. (2009) Dynamic nuclear polarization of <sup>13</sup>C in aqueous solutions under ambient conditions. *J. Magn. Reson.*, **201** (2), 137–145.
- 109** Griffin, R.G. and Prisner, T.F. (2010) High field dynamic nuclear polarization—the renaissance. *Physical Chemistry Chemical Physics*, **12** (22), 5737–5740.
- 110** Annino, G., Villanueva-Garibay, J.A., Bentum, P.J.M., Klaassen, A.A.K., and Kentgens, A.P.M. (2009) A High-Conversion-Factor, Double-Resonance Structure for High-Field Dynamic Nuclear Polarization. *Appl. Magn. Reson.*, **37** (1-4), 851–864.
- 111** Villanueva-Garibay, J.A., Annino, G., van Bentum, P.J.M., and Kentgens, A.P.M. (2010) Pushing the limit of liquid-state dynamic nuclear polarization at high field. *Phys. Chem. Chem. Phys.*, **12** (22), 5846.
- 112** van Bentum, P.J.M., van der Heijden,

- G.H.A., Villanueva-Garibay, J.A., and Kentgens, A.P.M. (2011) Quantitative analysis of high field liquid state dynamic nuclear polarization. *Phys. Chem. Chem. Phys.*, **13** (39), 17 831–17 840.
- 113** Denysenkov, V., Prandolini, M.J., Gafurov, M., Sezer, D., Endeward, B., and Prisner, T.F. (2010) Liquid state DNP using a 260 GHz high power gyrotron. *Phys. Chem. Chem. Phys.*, **12** (22), 5786–5790.
- 114** Denysenkov, V.P., Prandolini, M.J., Krahn, A., Gafurov, M., Endeward, B., and Prisner, T.F. (2008) High-Field DNP Spectrometer for Liquids. *Appl. Magn. Reson.*, **34** (3-4), 289–299.
- 115** Prandolini, M.J., Denysenkov, V.P., Gafurov, M., Endeward, B., and Prisner, T.F. (2009) High-Field Dynamic Nuclear Polarization in Aqueous Solutions. *J Am Chem Soc*, **131** (17), 6090–6092.